ADVANCED ENERGY & SUSTAINABILITY RESEARCH
www.advenergysustres.com

Synthesis of Pt Carbon Aerogel Electrocatalysts with Multiscale Porosity Derived from Cellulose and Chitosan Biopolymer Aerogels via Supercritical Deposition for Hydrogen Evolution Reaction

*Ala Alsuhile, Philip Sidney Pein, Şansim Bengisu Barım, Selmi Erim Bozbağ, Irina Smirnova, Can Erkey, and Baldur Schroeter**

The aim of this study is to investigate the activity and stability of carbon aerogel-supported platinum electrocatalysts in the hydrogen evolution reaction, compared to current solutions based on carbon black. Self-synthesized carbon aerogels (pyrolyzed cellulose, and chitosan-based aerogels) with multiscale porosity and high overall specific surface area (up to ≈2500 $m^2 g^{-1}$), as well as Vulcan XC-72R supports were loaded via supercritical deposition (SCD) with platinum nanoparticles (mean particle diameter ≈1.3–2.0 nm, 2.8–3.8 wt% Pt loading). Overpotentials ranged from 46.5 to 50.0 mV at 10 mA cm^{-2}, whereas self-synthesized electrocatalysts had similar overpotentials as compared to a commercial catalyst with ≈8–10 times higher Pt loading. In addition, Pt-carbon aerogel electrocatalysts had higher stability and durability as compared to Pt-Vulcan, most probably due to the high micro- to mesoporosity of carbon aerogels, which promotes nanoparticle stability. The current density at 40 mV for Pt-Vulcan decreased by 80% after 20 h, whereas an insignificant drop was observed for Pt-carbon aerogels. These results show that the applied combination of materials (biopolymer-based carbon aerogels) and loading method (SCD) are a promising approach for synthesizing stable electrocatalysts with reduced platinum content for green hydrogen production.

1. Introduction

Global energy demand is projected to grow by 30% by 2040, with CO_2 emissions reaching 35.7 gigatons under the New Policies Scenario, which is insufficient to prevent severe climate change impacts.[1] As a result, it is imperative to produce electricity from renewable sources such as solar and wind power. However, these sources are inherently dependent on time and weather conditions, which can limit their efficiency and applications.[2] One promising solution to overcome this limitation is the conversion of renewable energy into chemical energy. Due to its outstanding gravimetric energy density (142 MJ kg^{-1}, higher heating value), hydrogen has been emerging as a potential candidate.[3] Up to date, the majority of hydrogen is produced via methods such as steam methane reforming (SMR) and coal gasification (CG), which emit significant amounts of CO_2.[4] An alternative way to produce hydrogen with zero direct CO_2 emissions is the electrolysis of water: if the process is driven by renewable sources (such as solar or wind power), it contributes directly to reducing greenhouse gas emissions and aligns with the UN sustainability development goal (SDG) 7, which aims to ensure access to affordable, reliable, sustainable, and modern energy.[5]

Among different types of electrolyzers, alkaline electrolyzers and proton exchange membrane (PEM) electrolyzers have the highest technology readiness level (TRL) with PEM electrolyzers

A. Alsuhile, Ş. B. Barım, S. E. Bozbağ, C. Erkey
Department of Chemical and Biological Engineering
Koç University
Eng 105- Koç, Üniversitesi Mühendislik Fakültesi-Rumeli Feneri Yolu,
Sarıyer 34450, Istanbul, Turkey

The ORCID identification number(s) for the author(s) of this article can be found under https://doi.org/10.1002/aesr.202400433.

DOI: 10.1002/aesr.202400433

P. S. Pein, I. Smirnova, B. Schroeter
Institute of Thermal Separation Processes
Hamburg University of Technology
Eißendorfer Str. 38, 21073 Hamburg, Germany
E-mail: baldur.schroeter@tuhh.de

I. Smirnova, B. Schroeter
United Nations University Hub on Engineering to Face Climate Change at the Hamburg University of Technology
United Nations University Institute for Water, Environment and Health (UNU-INWEH)
21073 Hamburg, Germany

C. Erkey
Koç University Hydrogen Technology Center
Istanbul, Turkey

showing the important advantage of a fast response to changing power levels, rendering them the optimal choice to be coupled with dynamic energy sources like renewables.[6] H_2 is produced via the hydrogen evolution reaction (HER) at the cathode in the PEM electrolyzer. In HER, the adsorption of H^+ ions on catalytic sites should not be too strong (Gibbs energy (ΔG) < 0) to allow the release of H_2, nor too weak ($\Delta G > 0$) to ensure that the catalytic reaction occurs. Platinum (Pt) is the state-of-the-art catalyst for HER because the Gibbs free energy for adsorbed hydrogen molecules (ΔG_{H+}) on its active sites is near zero.[7–9] High costs and limited availability of Pt have motivated researchers to explore various strategies for the development of electrocatalysts with reduced Pt content.[10–13] One strategy is to use a support with a high surface area, which helps to disperse the Pt nanoparticles (Pt-NPs). Carbonaceous materials are commonly used due to their electrical conductivity and chemical inertness:[14] consequently various carbons have so far been investigated in HER as support materials as alternative to commercial carbon blacks with the aim to find materials which facilitate better dispersion and anchoring of Pt-NPs, including carbon nanotubes, carbon microspheres, and graphene.[15]

In general water electrolysis is still expensive due to the use of noble metals (e.g., Ru, Pt, and IrO_2) required in electrocatalysts: as a result, research directions are to replace them or reduce the loading amount.[16–23] The development of electrocatalysts with low Pt loading is therefore a key research direction for HER in PEM electrolyzers. However, such electrocatalysts often suffer from low stability and short durability due to the detachment and dissolution of Pt-NPs.[24–26] Despite these challenges, several studies have successfully developed highly stable electrocatalysts with Pt loadings of less than 5 wt%.[27–32] For instance, Pan et al. fabricated a highly stable, self-standing Pt single-atom catalyst anchored on a three-dimensional (3D) nitrogen-doped carbon tube grid, achieving a Pt loading of 1.04 wt%.[22] Similarly, Zhang et al. developed highly stable, self-supported Pt/MXene/carbon nanotube aerogels with a 3D vertically aligned porous structure, achieving a Pt loading of just 0.48 wt%.[23] In general, a high specific surface area (S_V), defects and high porosities support the anchoring and dispersion of Pt-NPs, while a continuous pore network facilitates the efficient transport of products and reactants.[33–35] For example, defects with precisely engineered vacancies in the graphene matrix served as anchoring sites, effectively trapping atomic Pt and significantly enhancing the stability and durability of the Pt–C3 catalytic configuration.[36] The presence of different sized pores (micropores with mean pore diameter $d_{pore} \leq 2$ nm, mesopores with $d_{pore} = 2$–50 nm and macropores with $d_{pore} \geq 50$ nm) within one material might therefore promote an overall high HER activity and enhance the catalyst stability as well. Furthermore, the support must be electrically conductive to minimize resistance to electron flow. Besides, doping carbonaceous materials with hetero atoms, such as nitrogen (N) and phosphorus (P) has been shown to improve the HER activity by creating anchoring sites for Pt-NPs and shifting the d-band center of Pt, thereby reducing the ΔG_{H+} and enhancing the catalytic performance.[37,38]

Carbon aerogels (CAs) with multiscale porosity have the potential to enhance the catalytic efficiency in comparison to commercial carbon blacks, as they provide a high microporous specific surface area for the anchoring and dispersion of Pt-NPs and an open and interconnected meso- to macroporous network for the efficient transport of products and reactants.[39,40] CAs are commonly produced by the pyrolysis of organic aerogels, which is performed under an inert gas atmosphere and at high temperatures. Due to its high mesoporosity, tailorability of pore size and pore volume, and high pyrolysis yield, resorcinol-formaldehyde (RF) aerogels have been the most common starting materials in the polymer-to-CA route since the 1990s.[41–43] With the increasing number of studies on biopolymer-based aerogels over the past decade, various examples of CAs with multiscale pore structure derived from biopolymer sources (e.g., cellulose, alginate, and chitosan) have been reported.[44–46] The use of cellulose (the most abundant biopolymer) and chitosan present potentially green alternatives to RF-based approaches, with chitosan belonging to the class of biopolymers, which naturally contain nitrogen. Not many studies report so far the application of cellulose derived CAs as catalyst supports. One example is the successful use of carbonized cellulose aerogels with a macro- to mesoporous pore texture as support for Pt-NPs: wet impregnation with H_2PtCl_6 followed by reduction resulted in a promising electrocatalyst for PEMFC cathodes with low platinum loading and good stability.[47] While this study highlights the potential of biopolymer aerogel-based CAs with multiscale porosity as catalyst supports, it is crucial to take the role of loading and reduction steps in the production process into account: in this case, three successive loading and reduction steps were necessary to achieve good activities and homogeneous Pt-dispersion/sufficient Pt-amounts. Only few studies report on the impact of CAs as supports for Pt in HER, whereas the use of the biopolymer CAs with regard to the particular differences in performance and effects of porosity and conductivity on HER have not been investigated at all.[37,48–51]

An approach to enhance the HER activity is to use Pt deposition methods free of organic solvents and capping agents, which may block the active sites of Pt-NPs.[52–54] One of these promising methods is supercritical deposition (SCD), which allows precise control of loading and nanoparticle size without the requirement of using additional organic solvents. SCD can be considered a particularly attractive technique in combination with aerogels, since the risk of meso- and micropore deformation or collapse during the impregnation of Pt precursor and during the depressurization is eliminated due to the absence of capillary forces in the supercritical state.[55–59] A comparison between two Pt-carbon black electrocatalysts synthesized by wet impregnation and SCD showed that Pt-NPs deposited by the latter method were more resistant to migration and agglomeration, even though underlying mechanisms were not clarified.[60] In a different study, Pt particles with low particle sizes (≈1.2–2.9 nm) showed a remarkable narrower average size distribution and less agglomeration in electrocatalysts synthesized by SCD.[59]

The synthesis of biopolymer derived Pt-CAs and their conversion to electrocatalysts via SCD has not been explored yet. In this study, we aim to evaluate the potential of these new materials as HER electrocatalysts with low Pt-loading. Specifically, we compare cellulose-CAs, chitosan-CAs with commercial carbon black (Vulcan XC-72R) as supports while assessing the importance of various material properties such as electrical conductivity, specific surface area, porosity, and the presence of naturally incorporated nitrogen in the case of chitosan. One primary objective is to address the question, to which extend CAs properties

can help to stabilize small Pt-NPs without the need for additional metals or doping with heteroatoms.

2. Experimental Section

2.1. Materials

Vulcan XC-72R was obtained from Cabot International. (1,5-Cyclooctadiene) dimethyl-platinum (II) ($Pt(cod)me_2$) with a purity of 97% (melting point: 100–105 °C), was purchased from Sigma-Aldrich. It had high solubility (2.96 mg cm^{-3}) in $scCO_2$ at 353 K and 15 bar.[61] Microcrystalline cellulose type II (Vivapure 101) was purchased from JRS Pharma GmbH & Co. KG. Chitosan was purchased from abcr GmbH Ger & INT. Carbon dioxide with a purity of 99.998%, hydrogen, and nitrogen were procured from Messer Ali gaz. Nafion 117 solution at a 5% concentration was sourced from Ion Solutions Inc. Sulfuric acid with a 95–98% concentration was employed as needed. Sodium hydroxide was purchased from Merck KGaA. Ethanol (EtOH) with ≥99.8% and acetic acid ≥99% were purchased from Carl Roth GmbH & Co. KG. All chemicals were used without further purification, except Vulcan XC-72R, which was pre-treated by heating it to 120 °C under a nitrogen (N_2) atmosphere before SCD experiments. A commercial Pt/C (Sigma-Aldrich) electrocatalyst containing 30 wt% Pt was used for comparisons. Deionized water with a resistance of 18.2 MΩ was used in all experiments.

2.2. Preparation of Cellulose- and Chitosan-Derived CAs

The cellulose and chitosan-derived CA particles were both synthesized using the same general procedure (**Figure 1**): 1) Dissolution of the respective biopolymer in aqueous solution and hydrogel particle production via dripping method; 2) Washing of hydrogel particles; 3) Solvent exchange from water to EtOH to obtain alcogel particles; 4) Supercritical drying of alcogels to obtain aerogel particles; and 5) Carbonization of aerogel particles. All details about the aerogel production steps and biopolymer aerogel properties are provided in the supporting information (Figure S1–S3, Table S1, Supporting Information).

2.3. Preparation of Supports and Electrocatalysts

To obtain CAs, cellulose and chitosan aerogel beads were carbonized in a custom-build quartz tube oven (Figure S4, Supporting Information). The pyrolysis was conducted under inert atmosphere with a constant flow of N_2 (flowrate ≈ 0.5 Nl min^{-1}). After placing the sample in the oven, the atmosphere was initially depleted of oxygen by flushing it for 30 min with nitrogen. Then a two-step heating program was started. In the first step, water was removed from the aerogels by raising the temperature from 20 to 100 °C with a heating rate of 10 °C min^{-1}, followed by a dwell time of 30 min. The subsequent carbonization of aerogels was carried out by heating up to a final temperature of 800 °C with a heating rate of 1 °C min^{-1}. After a dwell time of 60 min at 800 °C the active heating was turned off, and the oven was passively cooled down below 70 °C under constant nitrogen flow. Obtained CAs beads (Figure S1b, Supporting Information) were removed, ground and stored in sealed boxes prior to further analysis and processing.

The SCD method was employed to synthesize the different electrocatalysts (Figure 1, bottom). Initially, 200 mg of the selected support material (Vulcan, cellulose-CA, or chitosan-CA)

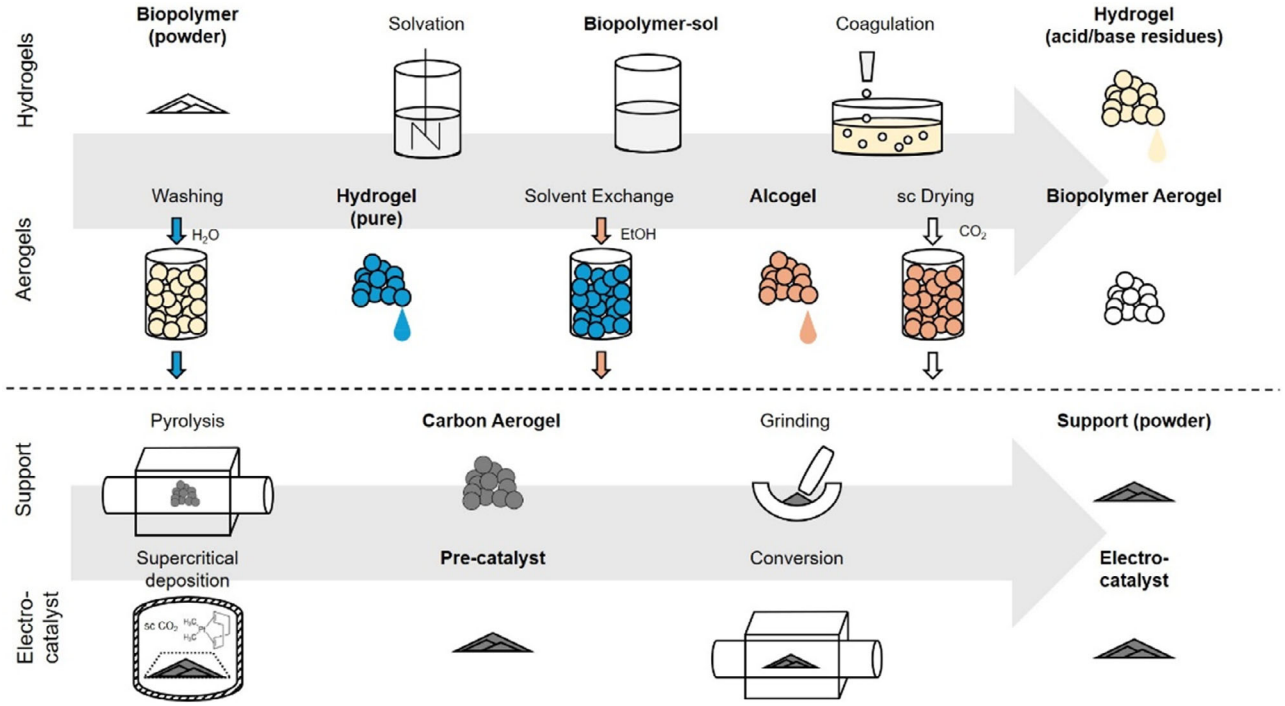

Figure 1. Scheme of process steps. Top: Production of biopolymer aerogels. Bottom: Production of CA supports and CA electrocatalysts.

and 20 mg of Pt(cod)me_2 were placed inside a custom-made high-pressure stainless-steel vessel with a volume of 57 mL. This vessel was equipped with two sapphire windows measuring 2.5 cm in diameter (Sapphire Engineering, Inc., Pocasset; MA). The deposition vessel underwent rapid pressurization and depressurization cycles using 0.13–0.16 MPa of carbon dioxide (CO_2) for 10 times to eliminate residual air inside. Subsequently, the temperature was increased to 80 °C during the experiments using a circulating heater/cooler (Cole-Parmer, Model 12 108-15). A syringe pump (ISCO Model 260D) was connected to the deposition vessel to pressurize CO_2 up to 15.53 MPa. The deposition vessel was kept at 80 °C and 15.53 MPa for 24 h.

Following this adsorption phase, the vessel was depressurized at a rate of 0.7 MPa min^{-1}, after which the impregnated support material was removed from the vessel. To convert the adsorbed Pt precursor into metallic Pt, the samples were placed within a quartz tube with an internal diameter of 220 mm, a wall thickness of 4 mm, and a length of 610 mm. This tube was placed inside a tube furnace (Thermolyne model F1125). Pt(cod)me_2 was converted at 200 °C for 4 h under constant N_2 stream (100 cm^3 min^{-1}, NTP). The tube was then cooled under flowing nitrogen.

2.4. Physical Characterization

Various characterization methods were used to investigate the physicochemical properties of the synthesized electrocatalysts. Textural characterization of materials was carried out via gas physisorption with N_2 5.0 at 77 K (mesopores) and CO_2 4.5 at 273.15 K (micropores). Constant temperatures during measurements were ensured by submerging the samples in liquid nitrogen (N_2 physisorption, 77 K) or water crushed-ice mixtures (CO_2 physisorption, 273 K). An overall sample mass of ≈20 mg was used in each run, and all samples were degassed at 60 °C (in case of aerogels) or 100 °C (in case of carbon supports and electrocatalysts) under vacuum (<7 mbar) for at least 6 h prior to each analysis. The respective isotherms were determined with a gas sorption analyzer (Nova 4200e, Quantachrome) by a manometric method from 5 mbar to ambient pressure. For aerogels, the Brunauer–Emmett–Teller (BET) method was applied in the p/p_0 range of 0.027–0.27 to estimate the specific surface area. The pore volume of the mesopores and the mean pore diameter were estimated via Barrett–Joyner–Halendia (BJH) method. The specific surface area, pore volume, and pore size distributions of CAs were derived by quenched-solid density function theory (QSDFT) methods (kernel: equilibrium isotherm, cylindrical pores) for N_2 isotherms and non-local density function theory (NLDFT) for CO_2 isotherms.

X-ray diffraction (XRD) analysis was performed using a Bruker D8 advance diffractometer equipped with a Cu Ka source within the 2θ range of 10°–90°. Pt loadings of all samples were quantified by using an Agilent 7700x ICP-MS instrument. X-ray photoelectron spectrometry (XPS) was employed for surface chemistry analysis, utilizing a Thermo-Scientific K-Alpha spectrometer with an Al anode (Al Ka = 1468.3 eV). The electron take-off angle was set at 90° between the sample surface and the axis of the analyzer lens. All binding energies were adjusted based on the C1s peak at 284.5 eV. XPS peak fitting was conducted using the XPS Avantage 5.9 software. A Renishaw Invia-Raman Microscope was utilized with a wavelength of 532 nm to understand the structural characteristics of both the unloaded and Pt-loaded supports. The morphology, Pt-NP size (based on an overall count number of 100 particles), and dispersion were investigated via scanning electron microscopy (SEM, ZEISS Ultra plus), and transmission electron microscopy (TEM, HITACHI HT7800 120 kV). SEM-imaging of non-coated samples was carried out under high vacuum at an accelerating voltage of 5.00 kV, a working distance of 5.7–6.0 mm using an in-lens detector. The electrical conductivity of powdered carbon supports was investigated using a resistivity measurement system (PD-51, Loresta GX, Mitsubishi Chemical Europe). The system is based on the four-pin measuring method of surface resistance at constant pressures between 1 and 10 kN. The nitrogen content in chitosan-CA was determined using an NCHS analyzer with internal thermal conductivity detector. The sample was freeze-dried prior to the analysis, which was carried out in duplicate.

2.5. Electrochemical Characterization

Electrochemical characterization of the samples was performed by employing a conventional three-electrode electrochemical cell connected to a potentiostat, Pine Instrument Company Model AFCBP1. The working electrode, provided by Pine Instruments, consisted of a glassy carbon disk with an internal diameter of 0.1963 cm^2. An Ag/AgCl reference electrode filled with a saturated KCl solution and a Pt wire as the counter electrode were used (provided by Pine Instruments). The chosen electrolyte was a 0.5 M H_2SO_4 solution. Electrocatalyst inks were prepared by dispersing 8 mg of the according electrocatalyst in 1 mL of isopropanol, 3 mL of distilled water, and 50 µL of a 5 wt% Nafion solution from Ion Solutions Inc. The mixture was sonicated in an ultrasonic water bath (Ultra-Turrax T25) for 30 min. Subsequently, 10 µL of the prepared ink was deposited onto the glassy carbon disk and allowed to air dry at ambient temperature and pressure overnight. Linear sweeping voltammetry (LSV) was conducted at a scan rate of 2 mV s^{-1} with rotating disk electrode (RDE) at 2000 rpm. All reported potentials were corrected using Equation (1). Cyclic voltammetry (CV) experiments were carried out at a scan rate of 50 mV s^{-1} within the potential range of 0.05–1.1 V versus the reversible hydrogen electrode (RHE).

$$E_{\mathrm{vs\cdot RHE}} = E_{\mathrm{vs\cdot Ag/AgCl}} + E^{\theta}_{\mathrm{vs\cdot Ag/AgCl}} + 0.059 \cdot \mathrm{pH} \quad (1)$$

3. Results

In this work, electrocatalysts were produced via supercritical deposition of Pt on three different carbon supports, based on: 1) CAs derived from cellulose aerogels (Pt-Cellulose-CA); 2) CAs derived from chitosan aerogels (Pt-Chitosan-CA); and 3) commercial carbon black (Pt-Vulcan). In the first part of this study, the textural and physical properties of the supports and

electrocatalysts are analyzed (Section 3.1) and in the second part their activity and stability in HER is evaluated (Section 3.2).

3.1. Physical Characterization of Supports and Electrocatalysts

Loading of carbon supports via SCD resulted in electrocatalysts with overall Pt-loading in the range of 2.8–3.8 wt% (**Table 1**). In the following, different properties of carbon supports and electrocatalysts are described in the order 1) textural properties; 2) size and dispersion of Pt-NPs; and 3) Properties of the carbon backbone related to electrical conductivity. In order to assess the (multiscale) porosity of supports and electrocatalysts, different techniques were used to analyze pores of various size regimes: the analysis of micropores in the range of pore diameters $d_{pore} = 0.35–1.5$ nm was based on CO_2-physisorption, mesopores (2–50 nm) were evaluated via N_2-physisorption and presence of larger macropores ($d_{pore} > 50$ nm) as well as homogeneity of the pore networks were verified via SEM. N_2-isotherms of all samples corresponded to type IV (IUPAC classification), with type H2 b) hysteresis, without plateaus at high relative pressures, indicating micro-/mesoporous structures with a broad pore-size distribution and a continuous transition to macropores (**Figure 2**a–c).[62] To clarify the effect of Pt loading on the pore texture of the different supports, the pore area distribution was normalized within each support type, respectively (Figure 2d–f). All samples showed a region of significant specific surface area provided by small mesopores (<10 nm), with peaks cut-off at the lower border of the model (2 nm) (Figure 2g). Our results demonstrated that the Pt-loaded electrocatalysts showed no large differences of their mesoporous structure as compared to their respective bare supports. One exception was the presence of new surface area provided by pores with sizes of 3 nm indicated in electrocatalysts (Figure 2d–f). From a fundamental point of view, this effect could be caused by either 1) the presence of small Pt-NPs attached on pore walls of pores with sizes of the same magnitude (therefore altering the overall pore-size), or 2) be an effect caused by the presence of Pt-NPs surface area itself. In the region of micropores, both aerogel-derived supports and electrocatalysts exhibited similar pore-size distributions (Figure 2h,i).

This indicates that the micropore morphology was independent of the initial biopolymer aerogel template and instead had a similar origin. Specifically, similar micropores were formed in both materials as defects etched into the carbon backbone's surface at higher pyrolysis temperatures.[63] In contrast to previous studies, which report a low micropore surface area of $82\ m^2\ g^{-1}$ in Vulcan XC-72R-based samples, our measurement repeatedly yielded noisy results, most probably due to a microporosity too low to be determined accurately with the applied method.[64] Consequently, we can state that CA supports provided significantly enhanced microporosity as compared to the commercial carbon black. In order to compare the pore properties of the supports and electrocatalysts in more detail, different intervals of pore sizes were defined and evaluated regarding the provided specific surface area (Table 1). Hereby, the micropore region is represented partially redundant, since N_2 measurements and CO_2 measurements overlap.

While CO_2 measurements are well-suited to determine small micropores (<1.5 nm), N_2 measurements reveal only large micropores, while being blind to smaller micropore fractions. Since the smallest micropore, which is assessable by N_2 measurements, should be generally material dependent, we chose to analyze the micropore region with both methods. For this particular use-case (anchoring of Pt-NPs) we chose to represent surface area in context of their pore sizes (slit widths and pore diameters) as a measure of the porous carriers' capacity to accommodate Pt-NPs. Overall, the cellulose-CA featured the significantly largest specific surface area, which originated mainly from micropores with diameters in the size range of up to 2 nm. The chitosan-CA had a significantly lower microporous specific surface area as compared to cellulose-CA, while all supports had moderate mesoporous specific surface areas in the overall range of $49–185\ m^2\ g^{-1}$. It has previously been reported that pores in the range of 4–7 nm could influence the activity of Pt/C electrocatalysts when mixed with an ionomer by allowing a segregation of Pt-NPs in small pores in which the ionomer might not be able to enter.[34] During HER activity tests, the three-phase system (Pt-Support-Nafion) is present where the diversity of multiscale pores in each support might impact the overall activity (see Section 3.2). Additional qualitative insight into textural properties of supports and electrocatalysts is provided by SEM as can be seen in **Figure 3**.

Table 1. Specific surface areas of supports and electrocatalysts (divided in pore-size intervals) and Pt-loading.

Material[a)] [–]	Pt loading[b)] [wt%]	S_V[c)] (<1.5 nm) [$m^2\ g^{-1}$]	S_V[d)] (<2 nm) [$m^2\ g^{-1}$]	S_V[d)] (2–10 nm) [$m^2\ g^{-1}$]	S_V[d)] (10–50 nm) [$m^2\ g^{-1}$]
Cellulose-CA	0	990	1440	89	8
Pt-cellulose-CA	3.8	892	1340	37	2
Chitosan-CA	0	613	176	43	83
Pt-chitosan-CA	2.8	473	163	140	45
Vulcan	0	(n. d.)[e)]	180	45	44
Pt-Vulcan	3.5	(n. d.)[e)]	190	34	38

[a)]Numbers given in round brackets correspond to the range of pore sizes, by which the according surface area is provided. Isotherms of CO_2 physisorption measurements are given in Figure S5, Supporting Information. [b)]A standard accuracy of the Pt loading via SCD of ±0.3 wt% was estimated based on repeating each loading process three times. [c)]Estimated via CO_2 physisorption at 273 K using a NLDFT model under the assumption of a slit-pore geometry. A relative standard deviation of 6% was estimated based on analyzing four individual batches. [d)]Determined via N_2 physisorption at 77 K using a QSDFT model under the assumption of a cylindrical pore geometry. A relative standard deviation of 9% was estimated based on analyzing four individual batches. [e)]n. d. = not detected.

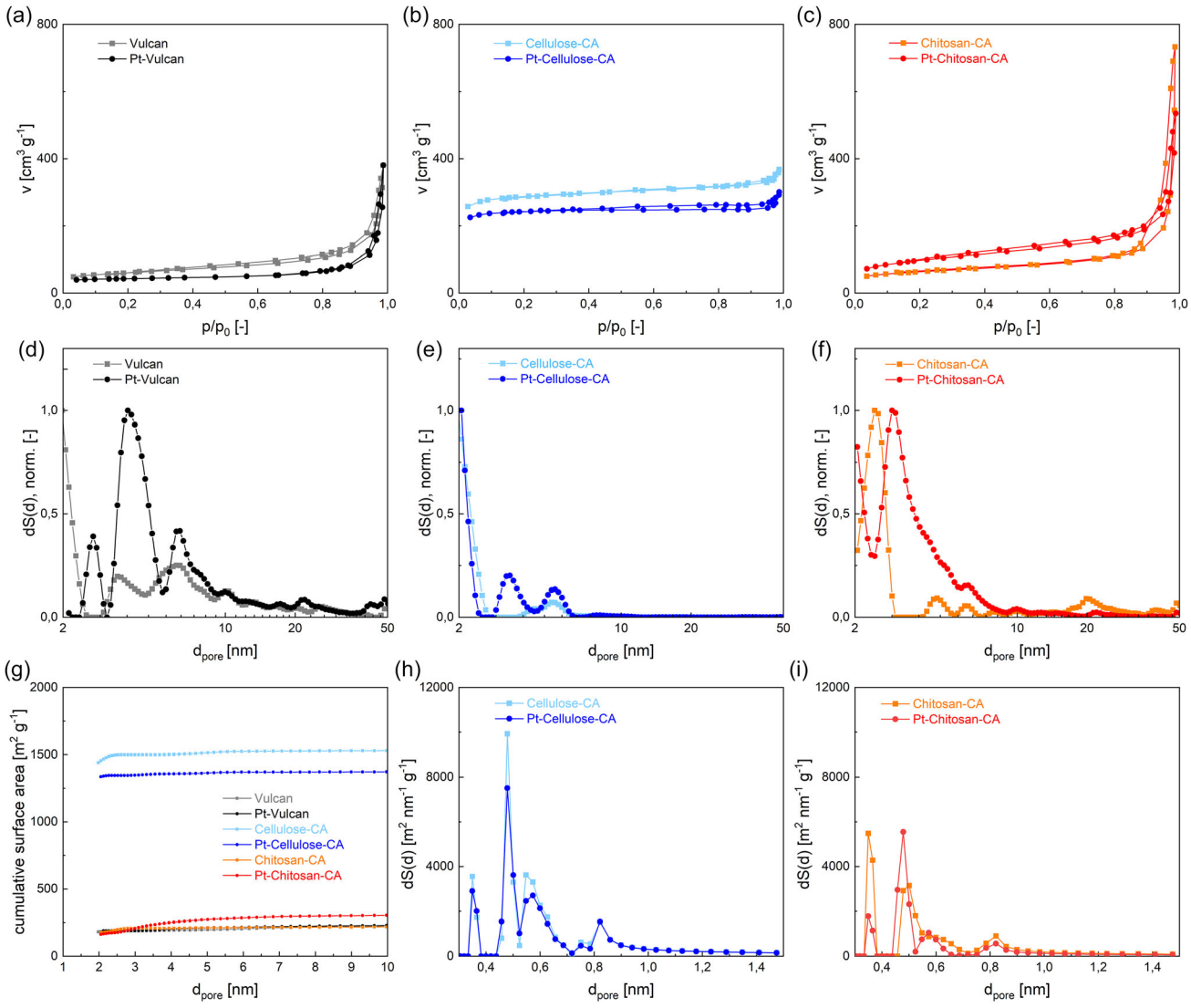

Figure 2. a–c) N_2-physisorption isotherms of supports and electrocatalysts, d–f) according pore-size distributions normalized per support type and g) cumulative surface areas. h,i) Micropore size distributions of aerogel support and electrocatalysts. Lines are drawn to guide the eye.

Continuous macroporous networks and some larger mesopores are visible in images of CA-supports, the latter being consistent with results from nitrogen sorption analysis. Since no significant differences between supports and electrocatalysts were detected via gas physisorption and SEM imaging, we conclude that the CA-aerogel structure was not harmed by either: 1) the SCD of Pt and 2) the grinding of the CA support prior to the SCD (see Figure 1). It is, however, notable, that the pore structures present in cellulose and chitosan CA (Figure 2, 3, Table 1) deviated from the pore structures, which were intrinsically present in the according biopolymers aerogels prior to their carbonization (Figure S2, S3, Table S1, Supporting Information). For instance, larger mesopores were lost during pyrolysis or converted to smaller ones. Such morphology changes are a logical consequence of the chemical conversion accompanied by mass loss and have already been reported; for example, for freeze-dried cellulose and chitosan-based materials).[45,65] Since numerous processes occur simultaneously or in quick succession during pyrolysis, details about particular influence factors behind the extend of pore loss and transformation are still to be clarified. Two key aspects are for example, the thermal decomposition of the organic matrix (leading to shrinkage and restructuring) and the release of volatile components (which might contribute to the formation of voids). Summarized, biopolymer aerogels produced in this work were usable as intrinsically porous templates for the production of CAs, which underwent—however—a significant morphological transformation during pyrolysis. While SEM imaging provided insights into larger-scale structural features of the different supports and electrocatalysts, TEM was used to reveal the Pt-NP size and distribution in each electrocatalyst. The Pt-NP size distributions were narrow with sizes below 4 nm in all cases, showing that a good dispersion of platinum was achievable via SCD independently of the support´s nature (**Figure 4**, for high-resolution TEM images

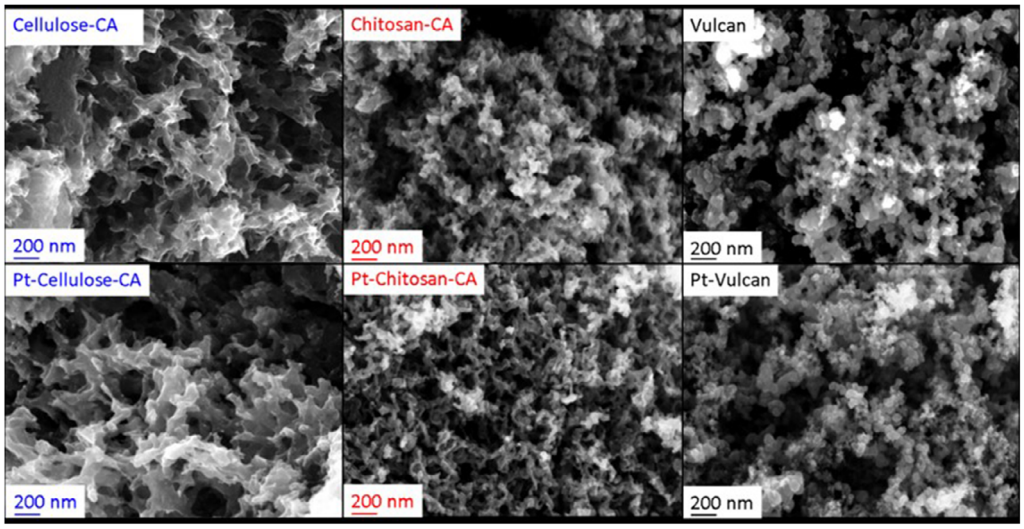

Figure 3. SEM images of the carbon backbone of bare supports (top) and electrocatalysts obtained after SCD and thermal conversion (bottom).

highlighting the size and crystalline nature of Pt-NPs we refer to Figure S6, Supporting Information).

Only small differences were detected between samples produced via SCD: the lowest mean Pt-particle size and narrowest distribution was achieved on Pt-cellulose-CA with the significantly highest overall specific surface area. In contrast, Pt-C 30 wt% had the largest mean particle size of 3.1 nm, the broadest size distribution and exhibited besides small nanoparticles also significantly larger Pt agglomerates >20 nm, which were even observable in SEM images (see Figure S7, Supporting Information). XRD analysis was employed to further analyze the Pt crystal structure, Pt particle size and the carbon structure of both supports and electrocatalysts (**Figure 5**). Two peaks around 24° and 44° were observed in all supports, indicating the presence of graphitic carbon.[66] The original peaks corresponding to crystal graphite, as defined in the Joint Committee on Powder Diffraction Standards (JCPDS) database (card no. 75-1621), were located at 26.5° and 44.3°.[67] The shifts to lower 2-theta values were indicative of the presence of amorphous carbon,[67] thus, XRD revealed the overall picture of carbon networks containing both: amorphous and graphitic moieties. Notably, the peak intensity around 44° was more pronounced in the cellulose-CA than the other supports. This elevated peak relative intensity around 44° suggested that cellulose-CA contained a higher graphitic carbon proportion than the other supports.[68,69] For chitosan-CA, the XRD diffraction results did not show a significant impact of nitrogen.

A similar pattern was observed after Pt loading, showing that SCD and conversion steps did not alter the intrinsic carbonic nature of the supports. Even though the presence of Pt on electrocatalysts was verified via elemental analysis and TEM imaging, no Pt peaks were detected via XRD on most samples: this result is likely to be attributed to the low-Pt loadings and small average sizes of Pt-NPs.[70] However, a minor peak was observed in Pt-Vulcan around the [111] plane at ≈40°. This suggests that the average Pt particle size was larger on the Vulcan support in comparison to cellulose-CA and chitosan-CA, which is consistent with the results from TEM imaging. One possible explanation for the differences in Pt-NP sizes could be rooted in the higher porosity (anchoring points) and specific surface area of the aerogel supports, which might lead to an increased Pt dispersion. In contrast, Pt peaks were clearly observable in the Pt-C 30 wt% sample, due to its significantly higher Pt loading. A Gaussian fit on the Pt (200) peak using Fityk software was performed to determine the full width at half maximum. By applying the Scherrer equation, the Pt particle (assumed spherical) size on Pt-C 30 wt%, was estimated to be ≈3.5 nm, which is comparable with the average particle size estimated from TEM images (3.1 nm) and suggests that the particle size distribution obtained by TEM is representative of the entire sample.

In additional analysis of the structural carbon characteristics via Raman spectroscopy, two prominent peaks, representing the D and G bands, were observed for both supports and catalysts (**Figure 6**, S8, Supporting Information).

The primary focus of the analysis was on the intensity ratio of these two peaks (ID/IG), which suggests the presence of relative defects or disorders within the graphitic structure.[71–73] In all samples, nearly identical ID/IG ratios verify the presence of a high degree of amorphous carbon (**Table 2**). In the case of cellulose-CA (Figure 6b), a slight increase to an ID/IG ratio of 1.26 indicated the presence of structural defects within the carbon matrix. A higher ID/IG ratio does not necessarily indicate lower graphitic content.[68,74] As observed in the XRD results, cellulose-CA exhibited higher graphitic content compared to Vulcan and chitosan, suggesting that the ID/IG ratio for cellulose-CA reflected greater disorder relative to its graphitic structure. Moreover, the ID/IG ratio remained almost constant following the Pt precursor adsorption in $scCO_2$ and the subsequent conversion to Pt at 200 °C, which is consistent with the findings obtained via other methods in this work. Investigation of the surface properties via XPS (Figure S9a,b and Table S2, Supporting Information) revealed as expected C1s and O1s signals in case of bare supports. In chitosan-CA, an overall amount of 11 wt% nitrogen was determined via elemental analysis. The presence

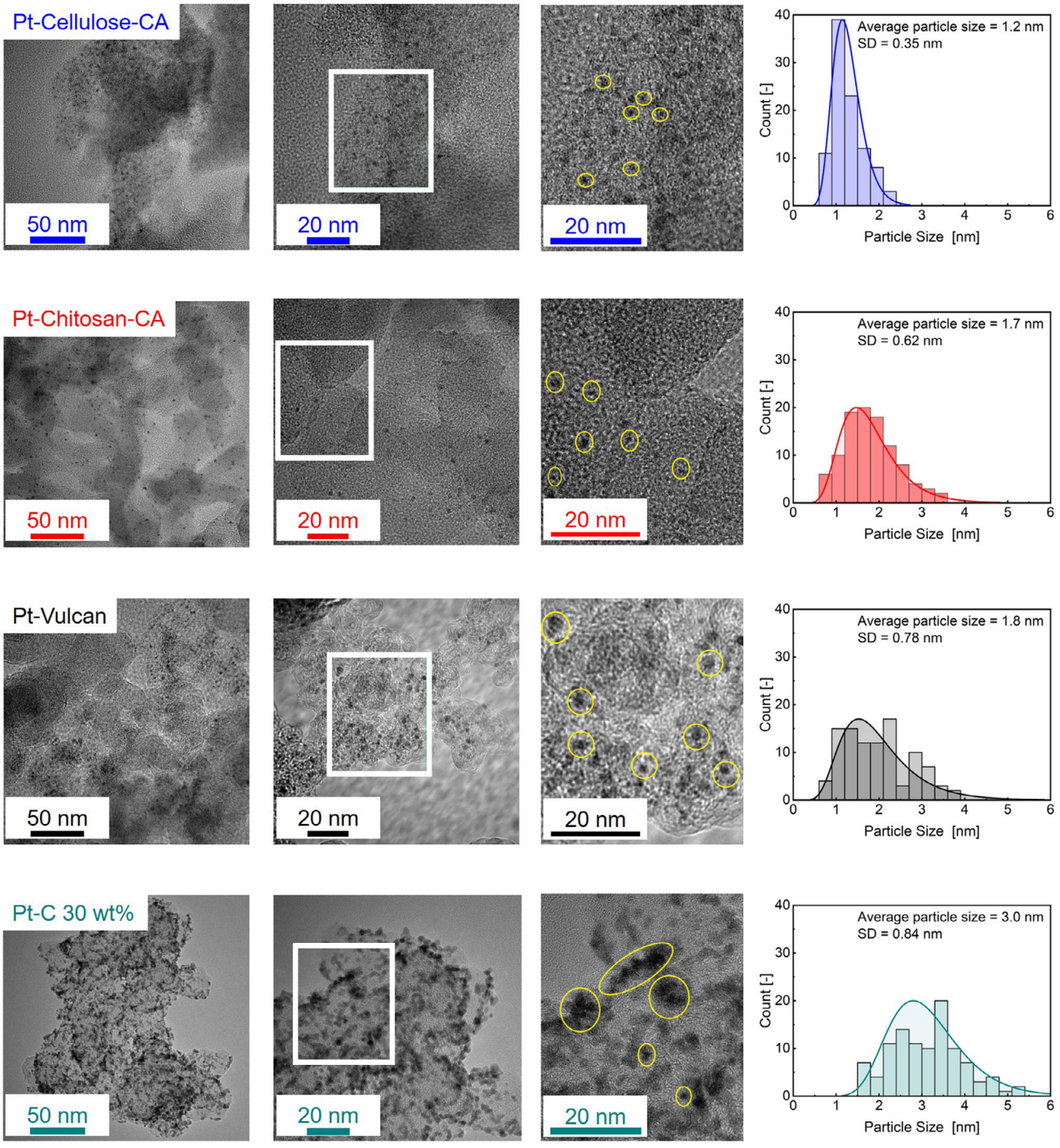

Figure 4. TEM images of self-synthesized and commercial Pt/C electrocatalysts and according Pt-NP size distributions (evaluated based on at least 100 Pt-NPs in each case). SD corresponds to the standard deviation of the mean particle diameter, evaluated via logarithmic fitting.

of nitrogen was also confirmed by the appearance of the N1s peak in the XPS survey. Remarkably, the C—C/C, O/C, and N/C ratios of the support materials showed no significant alteration compared to the Pt-loaded samples, showing that the chemical nature of the supports surface remained unchanged throughout processing. At high resolution (Figure S10, Supporting Information), C1s peaks of all bare supports could be deconvoluted to main three carbon peaks around 284.5, 286.4, and 288.6 eV corresponding to C—C (Sp3), C—O and C═O.[75] Chitosan-CA showed a slightly lower binding energy by 0.1–0.14 eV due to the presence of N, normally C—N is at 285.6 eV.[76,77] This was confirmed by deconvolution of the

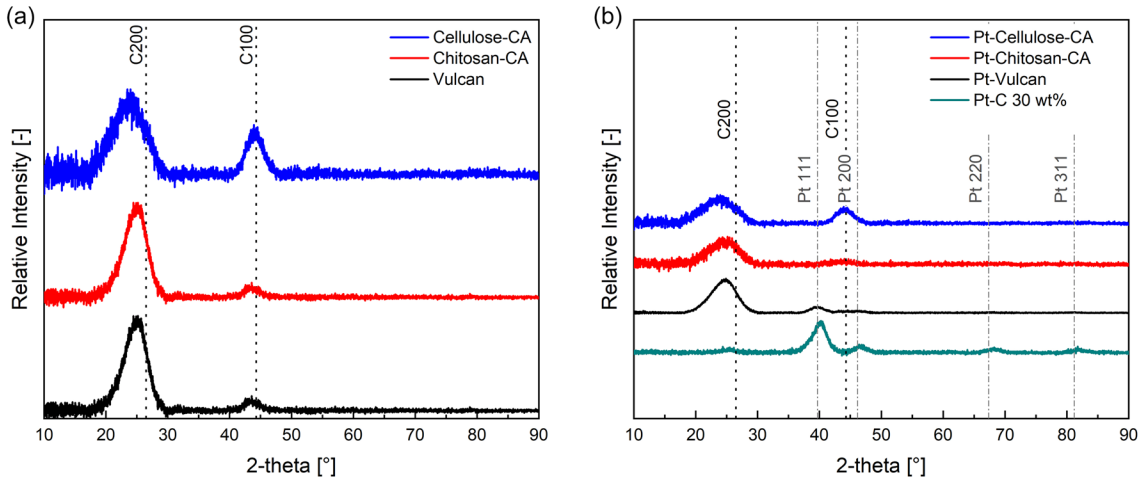

Figure 5. XRD patterns of a) bare supports and b) Pt containing electrocatalysts.

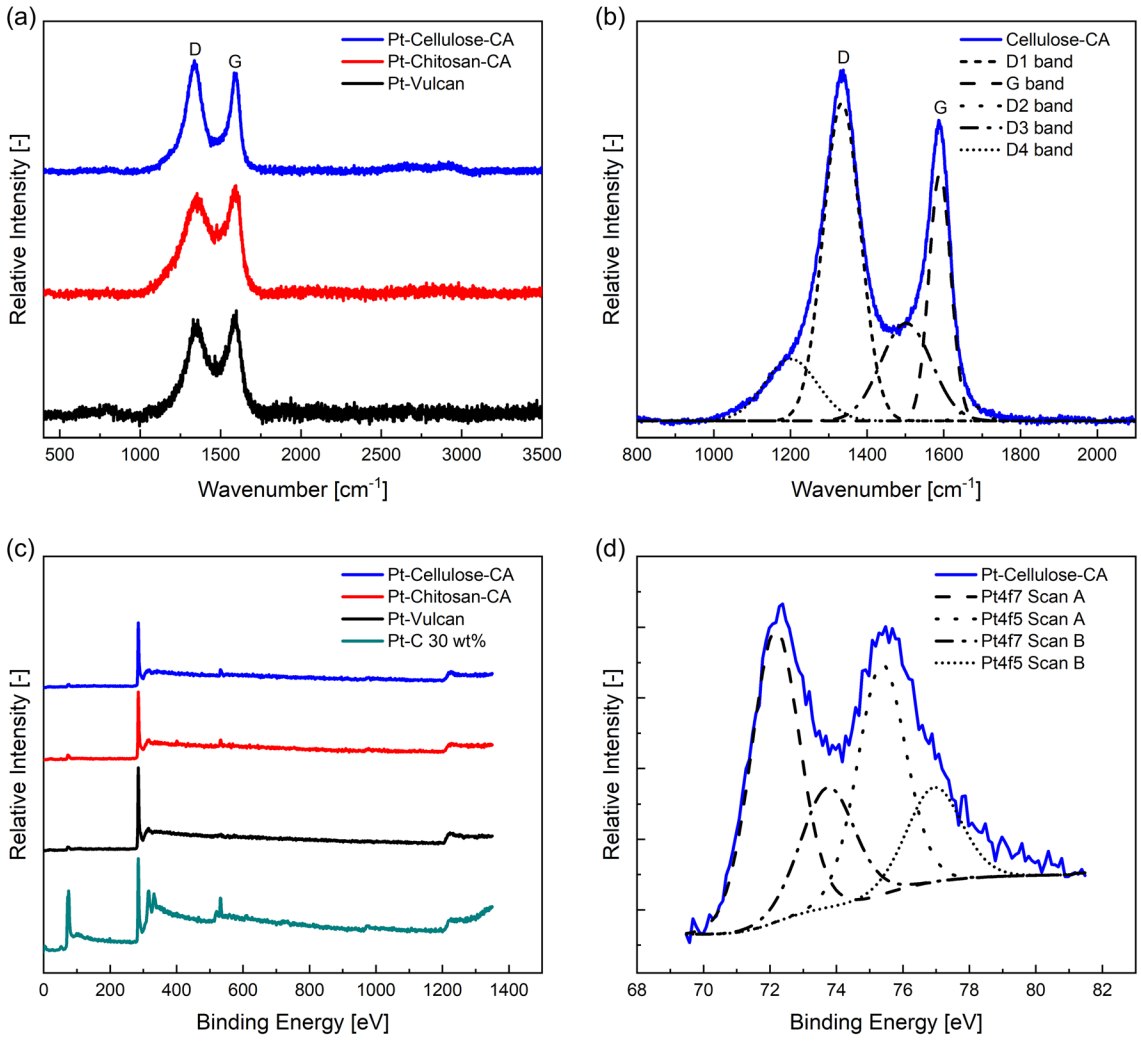

Figure 6. a) Raman spectra of electrocatalysts, b) peak deconvolutions of Pt-cellulose-CA, c) XPS analysis for the synthesized electrocatalysts, and d) Pt4f peak deconvolutions of Pt-cellulose-CA.

Table 2. ID/IG ratio of all samples.

Material	ID/IG support	ID/IG electrocatalyst
(Pt)-Cellulose-CA	1.29	1.26
(Pt)-Chitosan-CA	0.96	1.01
(Pt)-Vulcan	0.97	1.04

Ns1 in chitosan-CA that resulted in two mean peaks at 398.0 and 401 eV corresponding to pyridinic and graphitic N, respectively.[59] No significant shift in the C1s deconvoluted peaks were observed due to the Pt loading by SCD method. For Pt-chitosan-CA, the pyridinic N peak slightly shifted to higher value (by 0.1 eV), which could be due to the Pt–N interaction.

The Pt4F signal displayed two distinct peaks in all electrocatalysts (Figure S9c–f, Supporting Information). The more intense peaks at 72.2, 71.5, 71.9, and 71.6 eV for Pt-Cellulose-CA, Pt-Chitosan-CA, Pt-Vulcan, and Pt-C 30 wt%, respectively, indicated the presence of metallic Pt (Pt0) (71.6 eV).[78] The slight shift to higher binding energies for the metallic state could be attributed to the small particle size effect.[79] Though Pt-NPs were small in Pt-Chitosan-CA (similar to Pt-Vulcan, around 2 nm), the Pt0 peak was 71.5 eV, which indicated the effect of naturally doped N, that caused a lower shift in the Pt0 peak.[80] The less intense peaks in the range of 73–74 eV represented oxidized Pt species (Pt-OH, Pt-O). The metallic Pt form accounted for ≈70% of the total Pt content, signifying a predominance of metallic Pt, as reported previously.[81–83] The observation of oxidized Pt states in all electrocatalysts might be attributed to several factors. One key factor is the small size of the Pt-NPs, as it has been noted that decreasing Pt particle size leads to an increased amount of oxidized Pt species.[84,85] Moreover, Pt-NPs with weaker NP-support interactions are more prone to oxidation compared to strongly interacting particles.[86] In our case, synthesized electrocatalysts still possessed a similar proportion of Pt^0 despite lower Pt-NP sizes as compared to the commercial Pt-C 30 wt%, which is an indication for robust interactions between the carbon matrices and Pt-NPs obtained after SCD and thermal conversion.

Differences in the carbonic nature of the supports as well as textural properties might influence the electrical conductivity of the carbon backbone, hence affect the performance of the system. Measurements to determine the electrical conductivity σ were carried out with powdered supports under various pressures. It is notable, that the interpretation of σ for powdered samples is complex (as e.g., compared to monoliths) since the detected value depends on several factors: 1) The conductivity of the individual particles (intrinsic conductivity of the material); 2) The conductivity of the powder, which is compressed to a pellet by applying different pressures (pellet density). The pellet density depends on the contact between individual particles, which is influenced by many factors such as shape, size, compressibility, deformation behavior, and packing density).[87] As expected, σ was related to the applied pressure: higher values of σ were determined at higher pressures due to increased interparticle contact (**Figure 7**a). The electrical conductivities of the compressed materials differed by almost one order magnitude in the following order: σ Vulcan > σ cellulose-CA > σ chitosan-CA. Hereby, the trends for σ in dependence of pressure and resulting density were relatively similar for all samples, which speaks for a comparable deformation/compactation behavior in the applied pressure range (Figure 7a,b).

Even though chitosan-CA showed the highest pellet density, the overall detected σ-value was lower than for other supports (Figure 7b). Under the assumption that a higher pellet density correlates with higher interparticle contact, this result shows that chitosan-CA had indeed the lowest intrinsic material conductivity. The naturally included nitrogen in chitosan-CA seemed therefore to be present in a configuration, which did not enhance electrical conductivity.[88] One possible reason of the increase in electrical conductivity in cellulose-CA might be its higher graphitization degree (as determined by the prominent peak in the XRD at $2\theta = 44°$).

3.2. Electrochemical Characterization

HER activity of the synthesized electrocatalysts and commercial electrocatalyst Pt-C 30 wt% was examined by LSV (potential range: −153 to 219 mV vs RHE, scan rate of 2 mV s^{-1},

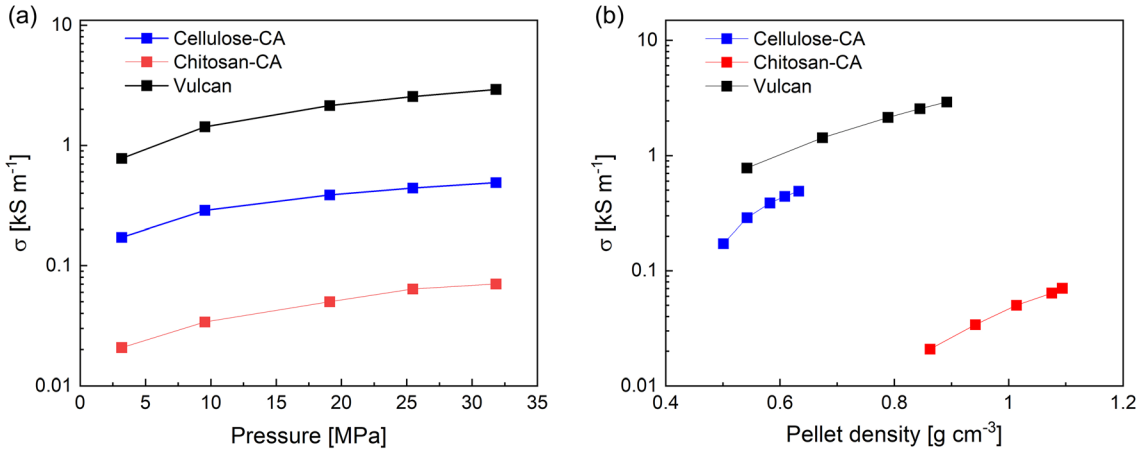

Figure 7. a) Electrical conductivity of supports in dependence of the applied mechanical pressure and b) resulting sample pellet density.

Figure 8a). Notably, all electrocatalysts exhibited an onset value potential near zero. The Tafel slope was similar for all the electrocatalysts, around 30 mV decade^{-1} (for Tafel plots we refer to Figure S11, Supporting Information). At a current density of 10 mA cm^{-2}, Pt-Cellulose-CA, Pt-Chitosan-CA, Pt-Vulcan, and Pt-C 30 wt% displayed overpotentials of 46.6, 49.5, 48.9, and 50 mV, respectively as can be seen in **Table 3**. Pt-Cellulose-CA exhibited the lowest overpotential value despite its absolute Pt loading on the glassy carbon being eight times lower than that of the commercial electrocatalyst. Notably, at low overpotentials, less than 60 mV, electrocatalysts synthesized by SCD showed slightly higher current density than the commercial electrocatalyst with 8–10 times higher Pt loading. Moreover, the electrochemical surface area (ESA) of all electrocatalysts, determined via cyclic voltammetry, ranged between 40 and 69 m^2 g_{Pt}^{-1} (detailed in Figure S12, Table S5, Supporting Information and according description).

The mass activity of the electrocatalysts was determined at three different overpotentials: 20, 40, and 60 mV (Figure 8b). At 40 mV, the estimated mass activity was 12 times greater for Pt-Vulcan and Pt-Cellulose-CA and 16 times higher for Pt-Chitosan-CA compared to Pt-C 30 wt%. The substantially higher mass activity for low loading Pt supported with carbonaceous material electrocatalysts compared to commercial Pt/C with loadings around 20–40% in LSV using RDE was also observed in some other studies reporting an inverse relationship between Pt loading and measured mass activity.[37,89,90]

This trend was attributed to HER activity being limited by the diffusion rates of H_2 and H^+ to and from the electrode surface.[89] It is suggested that the formation of H_2 gas bubbles at the electrode and their subsequent separation from the electrode within the catalytic layer into the electrolyte may negatively impact the diffusion rates of H_2 and H^+ and subsequently the measured mass activity of the electrocatalyst. Moreover, in most of the studies, the Tafel slopes were nearly constant around 30 mV dec^{-1} which indicated that the measured mass activities were not (material) intrinsic and HER is limited by diffusion rates.[89] Therefore, factors such as the thickness of the catalytic layer and support porosity, which influence diffusion rates, are likely to impact the measured mass activity. Additionally, competition between HER and hydrogen oxidation reactions (HOR) occurs at low potentials due to undiffused H_2 gas, leading to reduced measured mass activity.[91] The results obtained with the electrocatalysts synthesized in this study with low Pt loading also suggested that HER is limited by diffusion and the measured mass activities are not intrinsic.[89]

To further investigate the absence of kinetic limitations, a more dilute ink (same formula reported in the experimental section, with eight times lower mass of electrocatalyst) of Pt-C 30 wt% was prepared to reach a similar absolute Pt loading (4 μg$_{Pt}$ cm^{-2}) on the glassy carbon as for the synthesized electrocatalysts. Having the same electrocatalyst with different Pt loadings on glassy carbon eliminates the impact of factors such as active site types, particle size, and Pt dispersion on HER activity. This way, two layers with different thicknesses were formed from

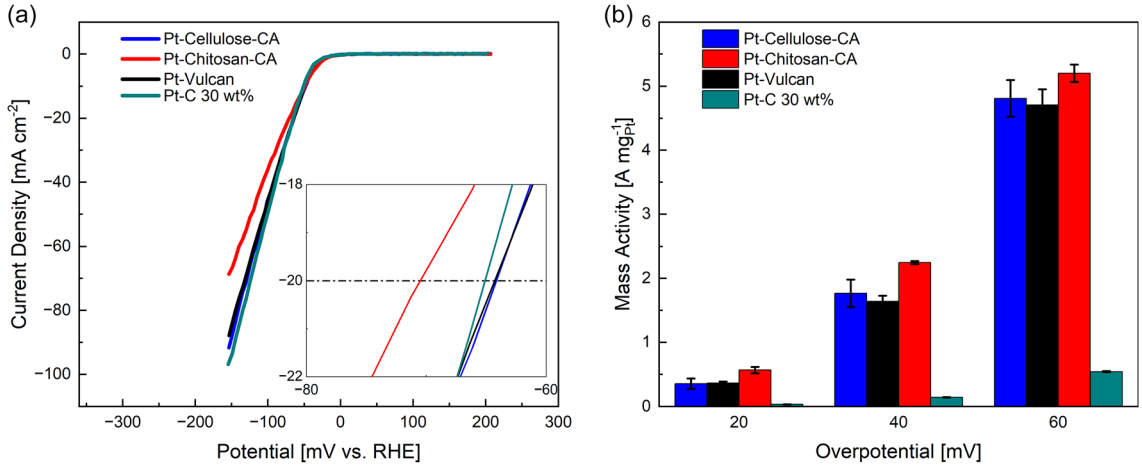

Figure 8. a) LSV analysis of electrocatalysts. Inset: magnified significant region of LSV analysis. b) Pt mass activity of different electrocatalysts. Error bars correspond to the standard deviation of averaged values from threefold determinations.

Table 3. Summary of electrochemical properties for the electrocatalysts.

Electrocatalyst	Pt-loading on GC [μg$_{Pt}$ cm^{-2}]	Pt-NP mean size [nm]	Tafel slope [mV dec^{-1}]	Overpotential@ 10 mA cm^{-2} [mV]	Mass activity@ 40 mV [A mg$^{-1}_{Pt}$]
Pt-cellulose-CA	3.8	1.2	28.6 ± 2.2	46.6 ± 1.6	1.8 ± 0.21
Pt-chitosan-CA	2.8	1.7	31.9 ± 1.8	49.5 ± 0.3	2.3 ± 0.02
Pt-Vulcan	3.5	1.8	30.2 ± 2.1	48.9 ± 0.9	1.6 ± 0.09
Pt-C 30 wt%	30	3.0	31.9 ± 0.8	50 ± 2.6	0.14 ± 0.01

the same electrocatalyst type. This decrease in Pt loading from 30 to 4 $\mu g_{Pt}\,cm^{-2}$ led to a drop in current density by 30% at an overpotential of 40 mV, which was expected since the amount of electrocatalyst was lowered. Nevertheless, the measured mass activity increased by 5.2-fold instead of staying constant (**Figure 9**) supporting the hypothesis that HER is entirely controlled by mass transfer limitations.[89] However, when the Pt loading of Pt-C (30 wt%) on GC was reduced to match that of the synthesized electrocatalysts, the current densities of the synthesized electrocatalysts were about 30% higher than those of Pt-C (30 wt%). This difference can be attributed to the large Pt-NP agglomerations observed in Pt-C (30 wt%), as can be seen in SEM images (Figure S7, Supporting Information). Aforementioned discussion on mass transfer limitation limiting HER activity clarifies, why there was no significant difference in the measured mass activity of the electrocatalysts synthesized in this study.

Electrochemical impedance spectroscopy (EIS) was performed at potential of −10 mV versus RHE between 200 kHz and 10 mHz. As can be seen in Figure S13, Supporting Information, Pt-Vulcan had slightly lower charge transfer resistance (Rct) compared to Pt-cellulose-CA. This difference in Rct could be explained due to the higher electrical conductivity of Vulcan compared to cellulose-CA (Figure 7).[92–95] Chitosan-CA had the highest resistance among the synthesized electrocatalysts, due its low conductivity and lower Pt loading. Despite its lower electrical conductivity, Pt-cellulose-CA demonstrated a slightly lower overpotential at 10 mA cm^{-2} than the Pt-Vulcan electrocatalyst. This raises questions about the role of electrical conductivity and porosity in HER performance when tested by the RDE method. This result indicated that the conductivity of cellulose-CA might be sufficient to ensure electron flow, and a higher conductivity of the support (like, e.g., for Vulcan) may not be necessary (especially in the given case of a thin electrocatalyst layer on the GC). Furthermore, multiscale pores in CAs may optimize the three-phase (Pt-support-Nafion) interaction to positively impact HER activity. Nevertheless, the impact of the porosity on HER activity tested by RDE method has not been investigated yet. Thus, due to the mass transport limitations, influence of

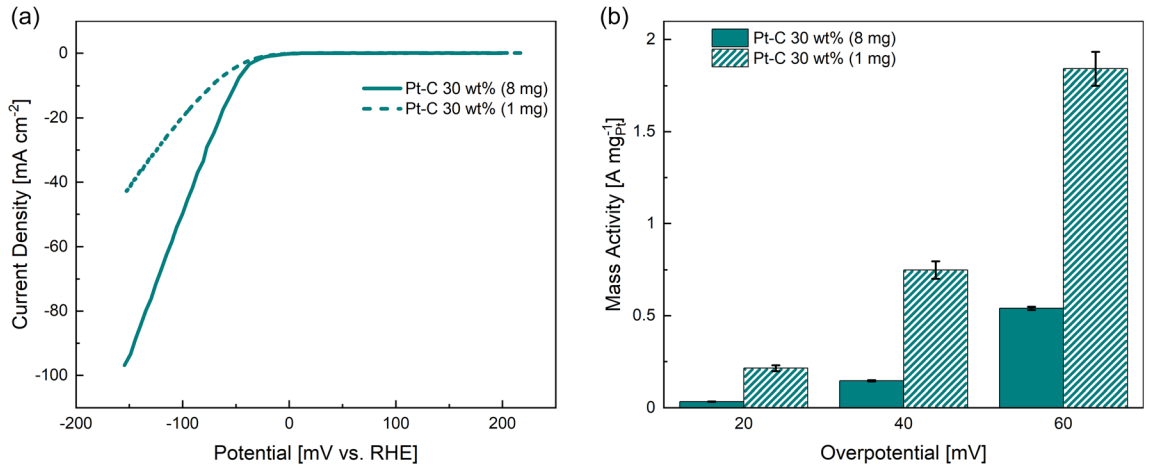

Figure 9. a) LSV analysis b) Pt mass activity of 1 and 8 mg of Pt-C 30 wt% in the ink formula to form two different thicknesses on the GC.

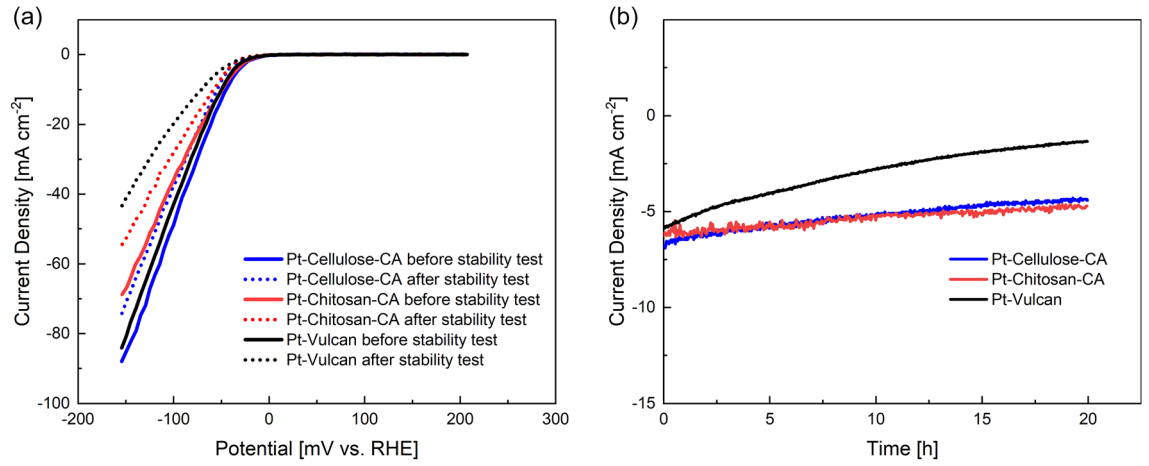

Figure 10. a) LSV test before and after 1000 cycles at 100 mV s^{-1} for the synthesized electrocatalysts, b) chronoamperometry test for the synthesized electrocatalysts at 40 mV, carried out for 20 h.

the supports' nature on the intrinsic activity of HER could not be quantified.

In contrast to HER activity, the impact of the different supports on electrocatalyst stability and durability could be clearly identified and proved to be particularly significant as seen in the stress and chronoamperometry tests. In the former, 1000 cycles were performed between −153 and 219 mV versus RHE at a scan rate of 100 mV s^{-1} for each electrocatalyst. LSV tests were carried out before and after this stress test, and the loss of activity was determined by the potential shift. An increase in potential at a specific current density indicates a decrease in HER activity. As depicted in **Figure 10**a and S14, Supporting Information, the potential shifts at 20 mA cm^{-2} for Pt-cellulose-CA, Pt-chitosan-CA, and Pt-Vulcan were 10.5, 11.3, and 34.07 mV, respectively and Pt-Vulcan experienced a threefold increase in potential shift compared to the CA-supported electrocatalysts.

From a fundamental point of view, several mechanisms could be responsible for the observed activity losses, including Pt-NP migration (leading to coalescence) and Pt dissolution (followed by Ostwald ripening or reformation of Pt in the ionomer phase).[96,97] Furthermore local carbon corrosion may induce direct Pt-NP detachment, while severe carbon corrosion could lead to significant morphological changes in the support, consequently altering internal mass transport.[96,97] To investigate the mechanisms behind the activity loss in this study, the catalyst

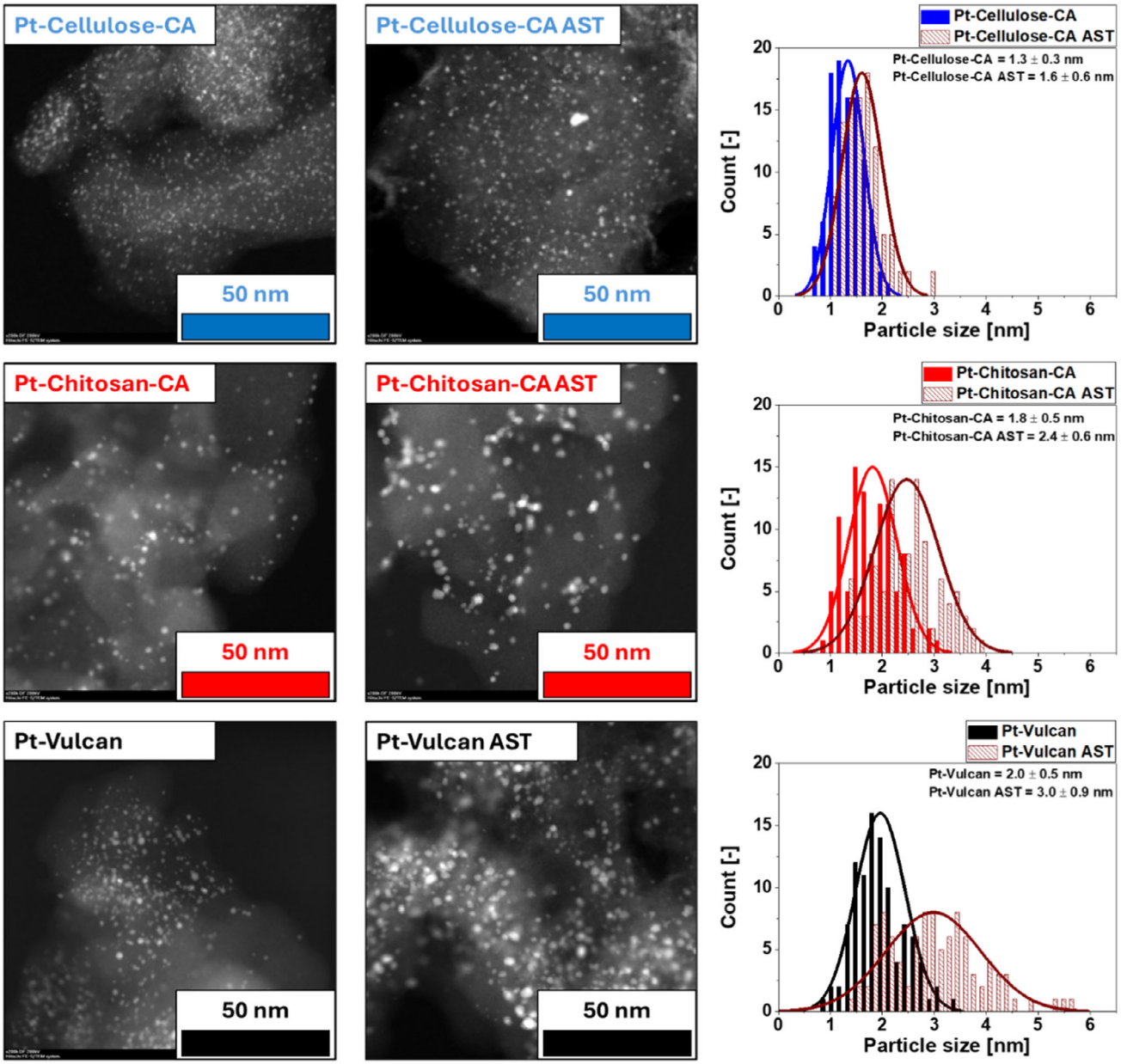

Figure 11. STEM images of synthesized catalysts before and after the stability test and their Pt-NP size distributions.

layer on the glassy carbon was carefully removed after the stress test and post analyzed via STEM imaging. No severe carbon corrosion was observed, which aligns with the reaction conditions: the electrolyte was saturated with N_2 for 30 min before testing, and a continuous N_2 atmosphere was maintained to prevent O_2 redissolution from the air. Across all electrocatalysts, an increase in Pt-NP mean diameter was detected −1.3, 1.8, and 2.0–1.6, 2.4, and 3.0 nm for Pt-cellulose-CA, Pt-chitosan-CA, and Pt-Vulcan, respectively—though no large agglomerates were found (**Figure 11**). This suggests that direct Pt-NP detachment played no significant role, as larger Pt-NPs are typically more prone to detachment due to their weaker interaction with the support. It can be inferred that the primary mechanisms causing the potential shift after the stability test were either coalescence or dissolution and Ostwald ripening, which result both in the loss of smaller Pt-NPs and formation of larger ones. Interestingly, although Pt-NP stability generally decreases with smaller particle sizes due to higher surface energy, the trend in this study was reversed: the electrocatalyst with the smallest Pt-NPs (Pt-cellulose-CA) exhibited the least particle growth. This contradicts the expected trend for Pt-NP dissolution and indicates, that support–Pt-NP interactions were decisive for the observed result. In this picture, pores acted as physical barriers, limiting Pt migration to some extent. The support with the highest specific surface area (cellulose-CA, see Table 1) provided the best Pt-NP stabilization, followed by chitosan-CA. In contrast, the absence of small meso- and micropores in the Vulcan support led to the largest potential shift and the most pronounced Pt-NP growth. In this context, it should be noted that an optimal size ratio between pores and Pt-NPs is required for effective pore confinement.[98] In our case, the Pt-NP sizes in Pt-cellulose-CA and Pt-chitosan-CA fell within the range of the support's pore sizes (see Figure 1e,f), suggesting that pore confinement played a key role in preventing Pt migration and coalescence. While Pt-NP dissolution cannot be entirely ruled out, our results suggest that this mechanism was not dominant, as dissolution is typically directly correlated to the initial Pt-NP size.

Given the significant amount of nitrogen being present in chitosan-CA, it is reasonable to assume, that nitrogen atoms in the carbon matrix may have further contributed to the formation of anchoring sites on a molecular level, as also indicated by XPS analysis (shift of pyridinic nitrogen). This interaction could principally help to prevent Pt-NP-migration in Pt-chitosan-CA and therefore compensate for its significantly lower surface porosity as compared to cellulose-CA.[37] However, more in-depth studies would be required to verify this effect. In order to assess the stability over a longer timeframe, a chronoamperometry test over 20 h was additionally conducted, where the potential was fixed, and the current density was measured as a function of time. Figure 10b displays the chronoamperometry test for the three synthesized electrocatalysts at 40 mV. Notably, the current density of Pt-Vulcan decreased by 80% within 20 h, indicating low electrocatalyst durability, while Pt-cellulose-CA and Pt-chitosan maintained largely constant current density, corroborating the results obtained from the stress test. Summarized, Pt-CA-based electrocatalysts exhibited comparable stability and durability, which were significantly enhanced as compared to Pt-Vulcan.

4. Conclusion

Green hydrogen is a sustainable renewable energy source, and its production reduces dependence on fossil fuels while promoting clean energy solutions for all. In addition to contributing to UN SDG 7 (Affordable and Clean Energy), green hydrogen production also supports SDG 13 (Climate Action), as it helps to reduce greenhouse gas emissions by utilizing renewable energy for hydrogen generation, contributing to global efforts to mitigate climate change. In this study, the unique structures of cellulose-CA and chitosan-CA, were for the first time combined with SCD to produce HER electrocatalysts with low Pt loading (3 wt%). Our key result is that the use of CA-supports helped to improve the stability of Pt-NPs significantly as compared to carbon black, without the need for additional metals or complex synthesis methods. It was demonstrated that the biopolymer-to-CA route resulted in multiscale porous supports with continuous, macroporous networks (enabling a good internal mass transport) and pronounced specific surface area provided by small mesopores and micropores. Hereby, SCD proved to be a powerful technique for preparation of CA-supported Pt-NPs, since it enabled homogenous distribution of Pt-NPs in the carbon matrix under preservation of the microstructural properties. The variation of the Pt-particle size in between different electrocatalysts was rather small despite the pronounced differences in the specific surface area of the supports, which shows the robustness of the SCD technique and low influence of micro- to mesopores on the resulting Pt dispersion. All electrocatalysts produced via SCD demonstrated similar HER activity as compared to a 30 wt% Pt-C commercial electrocatalyst (as reflected by the potential at a current density of 10 mA cm^{-2}). However, since mass transfer limitation entirely controls the HER activity, the measured mass activities were not intrinsic. A direct comparison between Pt-C (30 wt%) and self-synthetized catalysts (2.8–3.8 wt% Pt loading) showed their superior performance as compared to Pt-C (30 wt%) when both are measured with an equal amount of platinum loading on the GC. Specifically, the current densities of the synthesized electrocatalysts were ≈30% higher than those of the Pt-C (30 wt%). In addition to the microstructure, the electrical conductivity of the support role in the HER activity was investigated. Although the differences in σ between the samples spanned an order of magnitude with σ_Pt-Vulcan > σ_Pt-cellulose-CA > σ_Pt-chitosan-CA, Pt-cellulose-CA exhibited slightly higher current density compared to Pt-Vulcan at 10 mA cm^{-2}. This result indicated that the effect of electrical conductivity of the support on HER activity is negligible for these supports and needs further investigation. It is interesting to note, that the electrocatalyst stability was aligned with the trends of the different carbon supports meso- to microporosity (Pt-cellulose-CA > Pt-chitosan-CA > Pt-Vulcan), yielding higher stability in case of supports with higher specific surface area: it is therefore suggested that the presence of anchoring small meso- to micropores helped to improve the Pt-NP stability (e.g., by physical confinement in pores).

As a result of mass transfer limitations during the RDE measurements, a direct, quantitative comparison of our results with different studies can be inaccurate since each study employs different Pt loadings and experimental conditions. Comparison of the potential shifts (Table S6, Supporting Information) shows

that our synthesized electrocatalysts can compete with those from other studies, despite the absence of extrinsic doping, alloying, or non-green synthesis methods. While this study has been carried out in lab scale, the production process (including hydrogel production, supercritical drying, pyrolysis and SCD) has the potential for scale-up, particularly by incorporating a recycling system for the Pt precursor, which is the most expensive material involved.

Summarized, this proof-of-concept study highlights 1) the potential of bio-based CAs as supports in HER electrocatalysis, which contribute to Pt-NP stability due to beneficial Pt-NP-support interactions; 2) The effectiveness of SCD in producing homogeneously distributed and highly dispersed Pt-NPs throughout the CA network. Further optimization and understanding about the contribution of single influence factors could be achieved by investigation of the particular relationship between the carbon support's pore properties, Pt particle size, and HER stability. It is suggested that such materials are promising candidates for use as low-Pt-loading electrocatalysts in the production of green hydrogen using PEM electrolyzers.

Supporting Information

Supporting Information is available from the Wiley Online Library or from the author.

Acknowledgements

The authors are grateful for the financial support of TÜBİTAK with grant no. 221N284. They also acknowledge the support of Koç University Surface Science and Technologies Center (KUYTAM), Koç University TÜPRAŞ Energy Center (KUTEM), and Koç University Nanofabrication and Nanocharacterization Center for Scientific and Technological Advanced Research (n2STAR). The authors are also grateful for the financial support of the Federal Ministry for Economic Affairs and Climate Action (BMWK), grant no. KK5440301ZG1. The authors are grateful for the support in electrical conductivity analysis provided by Jessica Kroener (German Aerospace Center). Publising fees were supported by the Funding Programme Open Access Publishing of Hamburg niversity of Technology.

Conflict of Interest

The authors declare no conflict of interest.

Author Contributions

Ala Alsuhile: conceptualization (equal); investigation (lead); visualization (equal); writing—original draft (equal); writing—review & editing (equal). **Philip Sidney Pein**: data curation (lead); investigation (lead); visualization (supporting); writing—original draft (equal). **Şansim Bengisu Barım**: Investigation (supporting); Writing—review & editing (supporting). **Selmi Erim Bozbağ**: investigation (supporting); writing—review & editing (supporting). **Irina Smirnova**: funding acquisition (lead); supervision (supporting); writing—review & editing (supporting). **Can Erkey**: funding acquisition (lead); supervision (equal); writing—review & editing (supporting). **Baldur Schroeter**: conceptualization (equal); investigation (supporting); project administration (equal); writing—original draft (supporting); writing—review & editing (lead). **Ala Alsuhile** and **Philip Sidney Pein** contributed equally to this work.

Data Availability Statement

The data that support the findings of this study are available in the supplementary material of this article.

Keywords

aerogel, carbon, electrocatalyst, hydrogen evolution reaction, platinum, supercritical deposition

Received: December 22, 2024
Revised: February 18, 2025
Published online:

[1] International Energy Agency (IEA). World Energy Outloo, IEA, Paris **2017**.
[2] A. Vennila, S. Balambigai, V. Pradeepa, U. Sabari, V. Kavyashree, M. Jinisha, *Predicting Solar and Wind Power Production with the Weather Map Data Approach*, IEEE, Piscataway, NJ **2024**, pp. 1–6.
[3] L. Schlapbach, A. Züttel, *Nature* **2001**, *414*, 353.
[4] D. Gielen, E. Taibi, R. Miranda, *Int. Renewable Energy Agency* **2019**.
[5] N. Sánchez-Bastardo, R. Schlögl, H. Ruland, *Ind. Eng. Chem. Res.* **2021**, *60*, 11855.
[6] G. Zhao, K. Rui, S. X. Dou, W. Sun, *Adv. Funct. Mater.* **2018**, *28*, 1803291.
[7] B. Conway, G. Jerkiewicz, *Electrochim. Acta* **2000**, *45*, 4075.
[8] J. K. Nørskov, T. Bligaard, A. Logadottir, J. Kitchin, J. G. Chen, S. Pandelov, U. Stimming, *J. Electrochem. Soc.* **2005**, *152*, J23.
[9] R. Parsons, *Trans. Faraday Soc.* **1958**, *54*, 1053.
[10] Z. Li, R. Ge, J. Su, L. Chen, *Adv. Mater. Interfaces* **2020**, *7*, 2000396.
[11] F. Guo, T. J. Macdonald, A. J. Sobrido, L. Liu, J. Feng, G. He, *Adv. Sci.* **2023**, *10*, 2301098.
[12] X. Tian, P. Zhao, W. Sheng, *Adv. Mater.* **2019**, *31*, 1808066.
[13] F. Liu, C. Shi, X. Guo, Z. He, L. Pan, Z. F. Huang, X. Zhang, J. J. Zou, *Adv. Sci.* **2022**, *9*, 2200307.
[14] S. Sui, X. Wang, X. Zhou, Y. Su, S. Riffat, C.-J. Liu, *J. Mater. Chem. A* **2017**, *5*, 1808.
[15] J. Ding, H. Yang, S. Zhang, Q. Liu, H. Cao, J. Luo, X. Liu, *Small* **2022**, *18*, 2204524.
[16] Z. Wu, Q. Li, G. Xu, W. Jin, W. Xiao, Z. Li, T. Ma, S. Feng, L. Wang, *Adv. Mater.* **2024**, *36*, 2311018.
[17] P. Yang, F. Liu, X. Zang, L. Xin, W. Xiao, G. Xu, H. Li, Z. Li, T. Ma, J. Wang, *Adv. Energy Mater.* **2024**, *14*, 2303384.
[18] M. S. A. Sher Shah, G. Y. Jang, K. Zhang, J. H. Park, *EcoEnergy* **2023**, *1*, 344.
[19] Y. N. Zhou, W. L. Yu, H. J. Liu, R. Y. Fan, G. Q. Han, B. Dong, Y. M. Chai, *EcoEnergy* **2023**, *1*, 425.
[20] Y. Shen, W. Li, W. Wang, L. Xin, W. Xiao, G. Xu, D. Chen, L. Wang, F. Liu, Z. Wu, *Inorg. Chem. Front.* **2024**, *11*, 5508.
[21] B. Zhou, J. Wang, L. Guo, H. Li, W. Xiao, G. Xu, D. Chen, C. Li, Y. Du, H. Ding, *Adv. Energy Mater.* **2024**, *14*, 2402372.
[22] Q. Pan, Y. Wang, B. Chen, X. Zhang, D. Lin, S. Yan, F. Han, H. Zhao, G. Meng, *Small* **2024**, *20*, 2309067.
[23] X. Zhang, R. Wan, Y. Wang, X. Wu, H. Chen, Q. Pan, B. Chen, *Mater. Today Energy* **2024**, *43*, 101600.
[24] W. Zhai, Y. Ma, D. Chen, J. C. Ho, Z. Dai, Y. Qu, *InfoMat* **2022**, *4*, e12357.
[25] S. Anantharaj, P. E. Karthik, B. Subramanian, S. Kundu, *ACS Catal.* **2016**, *6*, 4660.
[26] S. Cherevko, *Curr. Opin. Electrochem.* **2018**, *8*, 118.

[27] H. Tian, X. Cui, L. Zeng, L. Su, Y. Song, J. Shi, *J. Mater. Chem. A* **2019**, *7*, 6285.
[28] S. Chakrabartty, C. S. Gopinath, C. R. Raj, *Int. J. Hydrogen Energy* **2017**, *42*, 22821.
[29] N. Roy, K. T. Leung, D. Pradhan, *J. Phys. Chem. C* **2015**, *119*, 19117.
[30] X. P. Yin, H. J. Wang, S. F. Tang, X. L. Lu, M. Shu, R. Si, T. B. Lu, *Angew. Chem. Int. Ed.* **2018**, *57*, 9382.
[31] Y. Mi, L. Wen, Z. Wang, D. Cao, H. Zhao, Y. Zhou, F. Grote, Y. Lei, *Catal. Today* **2016**, *262*, 141.
[32] J. Yu, D. Wei, Z. Zheng, W. Yu, H. Shen, Y. Qu, S. Wen, Y.-U. Kwon, Y. Zhao, *J. Colloid Interface Sci.* **2020**, *566*, 505.
[33] S. Ott, A. Orfanidi, H. Schmies, B. Anke, H. N. Nong, J. Hübner, U. Gernert, M. Gliech, M. Lerch, P. Strasser, *Nat. Mater.* **2020**, *19*, 77.
[34] V. Yarlagadda, M. K. Carpenter, T. E. Moylan, R. S. Kukreja, R. Koestner, W. Gu, L. Thompson, A. Kongkanand, *ACS Energy Lett.* **2018**, *3*, 618.
[35] X. Tuaev, S. Rudi, P. Strasser, *Catal. Sci. Technol.* **2016**, *6*, 8276.
[36] Q. Yang, H. Liu, P. Yuan, Y. Jia, L. Zhuang, H. Zhang, X. Yan, G. Liu, Y. Zhao, J. Liu, *J. Am. Chem. Soc.* **2022**, *144*, 2171.
[37] C. Wang, F. Hu, H. Yang, Y. Zhang, H. Lu, Q. Wang, *Nano Res.* **2017**, *10*, 238.
[38] H. Chen, X. Luo, S. Huang, F. Yu, Y. Chen, *J. Electroanal. Chem.* **2023**, *948*, 117820.
[39] A. Arenillas, J. A. Menéndez, G. Reichenauer, A. Celzard, V. Fierro, F. J. Maldonado Hodar, E. Bailón-Garcia, N. Job, A. Arenillas, J. A. Menéndez, *Organic and Carbon Gels: From Laboratory Synthesis to Applications*, Springer, Heidelberg, Germany **2019**, pp. 87–121.
[40] N. Shaari, S. K. Kamarudin, *Int. J. Energy Res.* **2019**, *43*, 2447.
[41] F. Li, L. Xie, G. Sun, Q. Kong, F. Su, Y. Cao, J. Wei, A. Ahmad, X. Guo, C.-M. Chen, *Microporous Mesoporous Mater.* **2019**, *279*, 293.
[42] Q. Abbas, M. Mirzaeian, M. A. Abdelkareem, A. Al Makky, A. Yadav, A. G. Olabi, *Int. J. Energy Res.* **2022**, *46*, 5478.
[43] A. Arenillas, J. A. Menéndez, G. Reichenauer, A. Celzard, V. Fierro, F. Maldonado Hodar, E. Bailón-Garcia, N. Job, in *Advances in Sol–Gel Derived Materials and Technologies* (Eds: M. Aegerter, M. Prassas), Springer Nature, Cham, Switzerland **2019**.
[44] Y. Hu, X. Tong, H. Zhuo, L. Zhong, X. Peng, S. Wang, R. Sun, *RSC Adv.* **2016**, *6*, 15788.
[45] P. Hao, Z. Zhao, Y. Leng, J. Tian, Y. Sang, R. I. Boughton, C. Wong, H. Liu, B. Yang, *Nano Energy* **2015**, *15*, 9.
[46] J. I. Del Río, L. Juhász, J. Kalmár, Z. Erdélyi, M. D. Bermejo, Á. Martín, I. Smirnova, P. Gurikov, B. Schroeter, *Nanoscale Adv.* **2023**, *5*, 6635.
[47] J. Rooke, C. de Matos Passos, M. Chatenet, R. Sescousse, T. Budtova, S. Berthon-Fabry, R. Mosdale, F. Maillard, *J. Electrochem. Soc.* **2011**, *158*, B779.
[48] M. Zhang, X. Xuan, X. Yi, J. Sun, M. Wang, Y. Nie, J. Zhang, X. Sun, *Nanomaterials* **2022**, *12*, 2721.
[49] W. Wang, Z. Pan, Z. Zhang, Y. Zhu, J. Shen, *ACS Appl. Nano Mater.* **2023**, *6*, 12150.
[50] L. Diao, C. Zhang, X. Yang, N. Zhang, J. Ren, D. Li, D. Yang, *Mater. Today Sustainability* **2023**, *23*, 100408.
[51] W. Liu, H. Zhu, L. Ying, Z. Zhu, H. Li, S. Lu, F. Duan, M. Du, *New J. Chem.* **2019**, *43*, 16490.
[52] X. Yang, Z. Lin, X. Cai, A. Cheng, Q. Zhang, Q. Meng, S. Qiu, W. Wang, L. Ma, L. Lin, *ChemNanoMat* **2021**, *7*, 1200.
[53] A. Han, Z. Zhang, X. Li, D. Wang, Y. Li, *Small Methods* **2020**, *4*, 2000248.
[54] J. Liu, X. Du, Y. Yang, Y. Deng, W. Hu, C. Zhong, *Electrochem. Commun.* **2015**, *58*, 6.
[55] S. B. Barim, E. Uzunlar, S. E. Bozbag, C. Erkey, *J. Electrochem. Soc.* **2020**, *167*, 054510.
[56] A. Bayrakçeken, A. Smirnova, U. Kitkamthorn, M. Aindow, L. Türker, İ. Eroğlu, C. Erkey, *J. Power Sources* **2008**, *179*, 532.
[57] A. Bayrakçeken, A. Smirnova, U. Kitkamthorn, M. Aindow, L. Tuerker, İ. Eroğlu, C. Erkey, *Chem. Eng. Commun.* **2008**, *196*, 194.
[58] F. E. S. Oztuna, S. B. Barim, S. E. Bozbag, H. Yu, M. Aindow, U. Unal, C. Erkey, *Electrochim. Acta* **2017**, *250*, 174.
[59] S. Ünsal, M. B. Yağcı, S. E. Bozbağ, B. Deljoo, M. Aindow, C. Erkey, *Energy Technol.* **2019**, *7*, 1900450.
[60] S.-Y. Ang, D. A. Walsh, *J. Power Sources* **2010**, *195*, 2557.
[61] O. Aschenbrenner, N. Dahmen, K. Schaber, E. Dinjus, *Ind. Eng. Chem. Res.* **2008**, *47*, 3150.
[62] M. Thommes, K. Kaneko, A. V. Neimark, J. P. Olivier, F. Rodriguez-Reinoso, J. Rouquerol, K. S. Sing, *Pure Appl. Chem.* **2015**, *87*, 1051.
[63] K. D. Henning, H. von Kienle, *Ind. Carbon Graphite Mater., Volume II* **2021**, *2*, 491.
[64] J. Zhang, X. Wang, C. Wu, H. Wang, B. Yi, H. Zhang, *React. Kinet. Catal. Lett.* **2004**, *83*, 229.
[65] C. Wan, Y. Lu, Y. Jiao, C. Jin, Q. Sun, J. Li, *Carbohydr. Polym.* **2015**, *118*, 115.
[66] S. S. Wang, Y. L. Xu, L. H. Zhang, Z. F. Liu, *Key Eng. Mater.* **2020**, *842*, 182.
[67] B. Matović, Y. E. Gorshkova, S. Y. Kottsov, G. Kopitsa, S. Butulija, T. M. Arsić, I. Cvijović-Alagić, *Diamond Relat. Mater.* **2022**, *121*, 108727.
[68] J. Xu, *Synth. Met.* **2023**, *295*, 117352.
[69] N. Hebalkar, G. Arabale, S. Sainkar, S. Pradhan, I. Mulla, K. Vijayamohanan, P. Ayyub, S. Kulkarni, *J. Mater. Sci.* **2005**, *40*, 3777.
[70] S.-Y. Lim, S.-I. Kim, M. S. Lee, S.-J. Bak, D. H. Lee, S.-H. Kwon, T. Kim, *Int. J. Hydrogen Energy* **2022**, *47*, 29456.
[71] S. Long, Y. Feng, F. He, S. He, H. Hong, X. Yang, L. Zheng, J. Liu, L. Gan, M. Long, *Carbon* **2020**, *158*, 137.
[72] Y. Feng, W. Jia, G. Yan, X. Zeng, J. Sperry, B. Xu, Y. Sun, X. Tang, T. Lei, L. Lin, *J. Catal.* **2020**, *381*, 570.
[73] S. Long, Y. Feng, Y. Liu, L. Zheng, L. Gan, J. Liu, X. Zeng, M. Long, *Sep. Purif. Technol.* **2021**, *254*, 117577.
[74] F. Maldonado-Hódar, C. Moreno-Castilla, J. Rivera-Utrilla, Y. Hanzawa, Y. Yamada, *Langmuir* **2000**, *16*, 4367.
[75] L. Jacobsohn, R. Schulze, M. M. Da Costa, M. Nastasi, *Surf. Sci.* **2004**, *572*, 418.
[76] J. Hu, C. Zhao, Y. Si, C. Hong, Y. Xing, Y. Wang, W. Ling, W. Feng, L. Feng, *Appl. Surf. Sci.* **2023**, *637*, 157910.
[77] Y. Qian, Z. Liu, H. Zhang, P. Wu, C. Cai, *ACS Appl. Mater. Interfaces* **2016**, *8*, 32875.
[78] A. Venezia, D. Duca, M. Floriano, G. Deganello, A. Rossi, *Surf. Interface Anal.* **1992**, *19*, 543.
[79] Z. Liu, L. M. Gan, L. Hong, W. Chen, J. Y. Lee, *J. Power Sources* **2005**, *139*, 73.
[80] Y. Chen, J. Wang, H. Liu, M. N. Banis, R. Li, X. Sun, T.-K. Sham, S. Ye, S. Knights, *J. Phys. Chem. C* **2011**, *115*, 3769.
[81] A. Guha, W. Lu, T. A. Zawodzinski, D. A. Schiraldi, *Carbon* **2007**, *45*, 1506.
[82] F. Şen, G. Gökağaç, *J. Phys. Chem. C* **2007**, *111*, 5715.
[83] B. Choi, H. Yoon, I.-S. Park, J. Jang, Y.-E. Sung, *Carbon* **2007**, *45*, 2496.
[84] F. Zaragoza-Martín, D. Sopeña-Escario, E. Morallón, C. S.-M. de Lecea, *J. Power Sources* **2007**, *171*, 302.
[85] A. Singh, K. Miyabayashi, *RSC Adv.* **2020**, *10*, 362.
[86] X. Wang, C. Zhang, B. Jin, X. Liang, Q. Wang, Z. Zhao, Q. Li, *Catal. Sci. Technol.* **2021**, *11*, 1298.
[87] J. Kröner, D. Platzer, B. Milow, M. Schwan, *Mater. Adv.* **2024**, *5*, 8042.

[88] M. Inagaki, M. Toyoda, Y. Soneda, T. Morishita, *Carbon* **2018**, *132*, 104.
[89] J. N. Hansen, H. Prats, K. K. Toudahl, N. Mørch Secher, K. Chan, J. Kibsgaard, I. Chorkendorff, *ACS Energy Lett.* **2021**, *6*, 1175.
[90] Z. Zeng, S. Küspert, S. E. Balaghi, H. E. Hussein, N. Ortlieb, M. Knäbbeler-Buß, P. Hügenell, S. Pollitt, N. Hug, J. Melke, *Small* **2023**, *19*, 2205885.
[91] J. Zheng, Y. Yan, B. Xu, *J. Electrochem. Soc.* **2015**, *162*, F1470.
[92] G. Wu, Y.-S. Chen, B.-Q. Xu, *Electrochem. Commun.* **2005**, *7*, 1237.
[93] F. Iskandar, O. B. Abdillah, E. Stavila, A. H. Aimon, *New J. Chem.* **2018**, *42*, 16362.
[94] M. S. Salas, V. Fuertes, D. A. Jaimes, N. Bajales, O. L. Pérez, *FlatChem* **2024**, *48*, 100766.
[95] S. Simon, P. Sreeja, *Energy Storage* **2024**, *6*, e70101.
[96] J. C. Meier, C. Galeano, I. Katsounaros, J. Witte, H. J. Bongard, A. A. Topalov, C. Baldizzone, S. Mezzavilla, F. Schüth, K. J. Mayrhofer, *Beilstein J. Nanotechnol.* **2014**, *5*, 44.
[97] J. C. Meier, I. Katsounaros, C. Galeano, H. J. Bongard, A. A. Topalov, A. Kostka, A. Karschin, F. Schüth, K. J. Mayrhofer, *Energy Environ. Sci.* **2012**, *5*, 9319.
[98] X. K. Wan, H. B. Wu, B. Y. Guan, D. Luan, X. W. Lou, *Adv. Mater.* **2020**, *32*, 1901349.